Available online at www.sciencedirect.com
ScienceDirect
Journal of Colloid and Interface Science 306 (2007) 368–378
JOURNAL OF Colloid and Interface Science
www.elsevier.com/locate/jcis

Drop manipulation and surgery using electric fields

L.Y. Yeo [a], R.V. Craster [b], O.K. Matar [c,*]

[a] *Micro/Nanophysics Research Laboratory, Department of Mechanical Engineering, Monash University, Clayton, VIC 3800, Australia*
[b] *Department of Mathematics, Imperial College London, South Kensington Campus, SW7 2AZ, UK*
[c] *Department of Chemical Engineering, Imperial College London, South Kensington Campus, SW7 2AZ, UK*

Received 15 June 2006; accepted 25 October 2006

Available online 28 October 2006

Abstract

We study the dynamics of a slender drop sandwiched between two electrodes using lubrication theory. A coupled system of evolution equations for the film thickness and interfacial charge density is derived and simplified for the case of a highly conducting fluid. The contact line singularity is relieved by postulating the existence of a wetting precursor film, which is stabilised by intermolecular forces. We examine the motion of the drop as a function of system parameters: the electrode separation, β, an electric capillary number, $\mathcal{C}$, and a spatio-temporally varying bottom electrode potential. The possibility of drop manipulation and surgery, which include drop spreading, translation, splitting and recombination, is demonstrated using appropriate tuning of the properties of the bottom potential; these results could have potential implications for drop manipulation schemes in various microfluidic applications. For relatively small β and/or large $\mathcal{C}$ values, the drop assumes cone-like structures as it approaches the top electrode; the latter stages of this approach are found to be self-similar and a power-law exponent has been extracted for this case.

Keywords: Thin films; Electric fields; Microfluidics; Spreading; Wetting; Lubrication

1. Introduction

Microfluidics has emerged from fluid mechanics as a field in its own right with a multitude of novel applications in biotechnology, e.g., point-of-care medical diagnostics, high throughput drug screening microarrays and biosensors (see, for instance, the recent review by Squires and Quake [1]). One area of significant interest within microfluidics is electrowetting in which small liquid volumes can be actuated or manipulated with the use of electric fields [2,3]. An example of this is the splitting or translation of drops, also known as drop surgery [4,5]. Such precise manipulation of fluids on the micro- and nanoscales will be essential in emerging "lab-on-a-chip" devices. The majority of the modelling studies of these electrowetting devices have involved quasi-static situations; a variety of such approaches have been adopted, e.g., thermodynamic [6], electromechanical [7,8], and contact line mechanics [9–11], amongst others [12].

The aim of the present article is therefore to generate a dynamic spreading theory capable of incorporating the contact angle and electric effects upon which electrowetting experiments can be modelled. The spreading dynamics of a conducting drop sandwiched between two plane parallel electrodes is therefore considered in which the potential at the bottom electrode is allowed to vary both spatially and temporally. The upper surface of the drop is assumed not to be in contact with the upper electrode initially; these two surfaces, however, could approach one another during the formation of so-called 'Taylor cones,' which occurs when the drop is attracted towards the electrode; these structures will be discussed briefly in the present work. We use lubrication theory to derive evolution equations for the interfacial thickness and charge density, which are solved numerically. Our numerical results show that the spatial and temporal potential variation facilitates a high degree of drop manipulation. These results therefore demonstrate the potential for performing these complex drop manipulations in electrowetting microfluidics.

With the advances in micro/nanofabrication techniques, it is now possible to pattern electrode surfaces to achieve such

* Corresponding author.
E-mail address: o.matar@imperial.ac.uk (O.K. Matar).

0021-9797/$ – see front matter
doi:10.1016/j.jcis.2006.10.063

spatial variations in the electric potential. Large voltage drops have been obtained along thin and long wire electrodes [13]; we anticipate the possibility of using a planar-like wire design in this case. Bader et al. [14] provide a method for the fabrication of electrodes to generate a spatial potential distribution; combined with a time-varying applied potential, this was exploited for microparticle separation. Spatial variations in the potential can also be obtained by patterning a thin non-uniform dielectric layer thickness. It is also possible to obtain spatial variations in the local effective electrokinetic (zeta-) potential of the substrate by using capacitance effects arising from embedded shielding electrodes in an analogous fashion to the electronic field-effect transistor [15–19]. Alternatively, we envisage the possibility of fabricating thin (both in thickness and in width) strips of dielectric layers. By carefully selecting the dielectric material of each adjacent layer based on their permittivities, it is possible to obtain a discrete spatial permittivity (and hence potential) distribution. In the limit of infinitely thin widths, it would then be possible to obtain a continuous distribution. Another possibility of obtaining spatial potential distributions is to employ shear horizontal surface acoustic waves generated by fabricating thin interdigitated transducers on a polished piezoelectric substrate [20]; this is commonly used to generate spatially periodic electrical potentials on the surface of substrates in interdigital dielectrometry for various sensing applications [21]. This speculative article is therefore intended to spur further investigations in this respect.

The remainder of the article is organised as follows. In Section 2, we provide brief details of the governing equations and the associated boundary conditions that define the problem and non-dimensionalise these to obtain a set of evolution equations that govern the interfacial drop height and charge. In addition, we also discuss the treatment of the contact line region. In Section 3, we present the results of our simulations for the constant and varying spatial potential cases, the latter consisting of linear and non-linear potentials; the limitations of the current model are also discussed in this section. Finally, we present our concluding remarks in Section 4.

2. Formulation

2.1. Governing equations

We consider the dynamics of a conducting, incompressible, Newtonian liquid drop of equilibrium thickness, $\mathcal{H}$, and length, $\mathcal{L}$, in a rectangular coordinate system $(x, 0, z)$; x and z denote the horizontal and vertical coordinates, respectively. The drop, which has velocity $\mathbf{u} = (u, 0, w)$, in which u and w are the horizontal and vertical components of $\mathbf{u}$, respectively, is bounded from below at $z = 0$ by a horizontal, flat, infinitely long rigid substrate, which acts as an electrode, and from above by an essentially inviscid gas that is overlaid by another electrode at $z = b$; the air–liquid interface is therefore located at $z = h(x, t)$. The interface is endowed with surface tension, γ, which is assumed to be constant. Interfacial charge q is also allowed to evolve via the following transport equation:

$$q_t + \mathbf{u}\cdot\nabla_s q - q\mathbf{n}\cdot(\mathbf{n}\cdot\nabla)\mathbf{u} = (\sigma_l\mathbf{E}_l - \sigma_g\mathbf{E}_g)\cdot\mathbf{n}, \tag{1}$$

in which t is the time, $\nabla_s = \nabla\cdot(\mathbf{I} - \mathbf{nn})$ the surface gradient operator, σ_i $(i = g, l)$ the conductivities of the phases, and $\mathbf{E}_i$ $(i = g, l)$ is the electric field, assumed to be solenoidal and irrotational such that

$$\nabla\cdot\mathbf{E}_i = \nabla^2\psi_i = 0 \quad (i = g, l), \tag{2}$$

where ψ_i denotes the electrode potential in phase i. In the above, $\mathbf{I}$ is the identity tensor and $\mathbf{n} = (-h_x, 1)/(1 + h_x^2)^{1/2}$ denotes the outward pointing unit normal to the interface. The subscripts x and t represent partial derivatives with respect to these variables, unless stated otherwise.

A voltage difference is applied between the two electrodes: the top electrode is grounded, i.e.,

$$\psi_g = 0 \quad \text{at } z = b, \tag{3}$$

and the potential at the bottom electrode is allowed to be constant, or spatially and temporally varying:

$$\psi_l = \psi_0\Psi(x, t) \quad \text{at } z = 0. \tag{4}$$

Here, ψ_0 represents the average value of the potential at the bottom electrode and $\Psi(x, t)$ the applied constant or variable potential. The presence of a thin dielectric layer, if any, above the bottom electrode will be ignored; the field lines through the dielectric layer given its low permittivity in most cases will always be straight and normal to both its interface with the conducting drop and the electrode, and so its presence can simply be accounted for by augmenting the potential drop across the electrodes. In addition, the aspect ratio of the drop is considered to be small, $\delta \equiv \mathcal{H}/\mathcal{L} \ll 1$, which will permit use of lubrication theory.

The model is therefore similar to that for two stratified thin dielectric films trapped between horizontal planar electrodes [22] in the limit of small viscosity ratios such that the bottom liquid layer is bounded from above by an inviscid gas phase. The reader is thus referred to the full derivation of the model in [22]. Here, we will only highlight the differences between the model and state the final evolution equations for the film height and interfacial charge that will be used in our simulation.

To account for the presence of a contact line, we allow for an additional term

$$\Pi = \frac{\mathcal{B}}{h_\infty^n}\left[\left(\frac{h_\infty}{h}\right)^n - \left(\frac{h_\infty}{h}\right)^m\right], \tag{5}$$

to capture the effects of the disjoining pressure as an energy per unit volume term in the momentum conservation equation, i.e.,

$$\rho(\mathbf{u}_t + \mathbf{u}\cdot\nabla\mathbf{u}) = -\nabla(p - \Pi) + \mu\nabla^2\mathbf{u}, \tag{6}$$

in which ρ and μ denote the liquid density and viscosity, and p and t represent the pressure and time, respectively; gravitational forces have been neglected. In Eq. (5), $\mathcal{B}$ is a dimensionless parameter which controls the relative significance of disjoining pressure effects; the first and second terms on the right-hand side of Eq. (5) represent the short-range repulsive and long-range attractive forces, respectively, with $(n, m) = (4, 3)$. We provide below (Section 2.2) details of the use of the disjoining

pressure in relieving the potential singularity at the contact line by postulating the existence of a thin precursor film of thickness h_∞ stabilised by antagonistic intermolecular forces [23].

We scale the problem to render the governing equations dimensionless using the following transformations:

$$x = \mathcal{L}\tilde{x}, \qquad (z,h) = \mathcal{H}(\tilde{z},\tilde{h}), \qquad u = \mathcal{U}\tilde{u},$$
$$w = \delta\mathcal{U}\tilde{w}, \qquad t = \left(\frac{\mathcal{L}}{\mathcal{U}}\right)\tilde{t}, \qquad p,\Pi = \left(\frac{\mu\mathcal{U}\mathcal{L}}{\mathcal{H}^2}\right)(\tilde{p},\tilde{\Pi}),$$
$$\psi = \psi_0\tilde{\psi}, \qquad q = \left(\frac{\epsilon_0\psi_0}{\mathcal{H}}\right)\tilde{q}, \tag{7}$$

where $\mathcal{U} = \delta^3\gamma/\mu$ is a characteristic velocity and ϵ_0 is the permittivity of free space; the tilde decoration denotes dimensionless quantities, which we shall drop henceforth.

It can then be shown [22] that upon substitution of these scalings into the governing equations and boundary conditions, the following leading order evolution equations for $h(x,t)$ and $q(x,t)$ can be derived:

$$h_t + \left(\tau\frac{h^2}{2} - \frac{h^3}{3}[p-\Pi]_x\right)_x = 0, \tag{8}$$

$$q_t + \left(\tau h - \frac{h^2}{2}[p-\Pi]_x\right)_x = \Sigma_g A_1 - \Sigma_l A_2, \tag{9}$$

where

$$A_1(x,t) = \frac{qh + \epsilon_l\Psi(x,t)}{\epsilon_l(h-\beta) - \epsilon_g h},$$
$$A_2(x,t) = \frac{q(h-\beta) + \epsilon_g\Psi(x,t)}{\epsilon_l(h-\beta) - \epsilon_g h}, \tag{10}$$

in which ϵ_i $(i = g,l)$ is the dielectric constant of phase i, $\beta \equiv b/\mathcal{H}$ is a dimensionless electrode separation and $\Sigma_i \equiv (\sigma_i\mathcal{L}/\epsilon_0\mathcal{U})$ $(i = g,l)$ are dimensionless conductivities, ratios of flow and charge relaxation time scales. In Eqs. (8) and (9), $\tau = \mathcal{C}q[(\beta-h)A_1]_x$ denotes the electrically-induced interfacial stress, in which $\mathcal{C} \equiv \epsilon_0\psi_0^2\mathcal{L}^2/\gamma\mathcal{H}^3$ is an electric capillary number, representing the ratio of electric to surface tension forces.

For large liquid conductivities, $\Sigma_l \gg 1$, it is possible to solve for q, i.e., through $A_1 \sim 0$:

$$q \approx \frac{\epsilon_g\Psi(x,t)}{\beta - h}, \tag{11}$$

and the potentials reduce to

$$\psi_l \approx \Psi(x,t), \qquad \psi_g \approx \left(\frac{z-\beta}{h-\beta}\right)\Psi(x,t), \tag{12}$$

while, further assuming $\epsilon_l \gg 1$, τ and p become

$$\tau \approx -\epsilon_g\mathcal{C}\frac{\Psi(x,t)}{(\beta-h)}\Psi_x,$$
$$p \approx -h_{xx} - \Pi - \frac{\epsilon_g\mathcal{C}}{2}\left(\frac{\Psi}{[\beta-h]}\right)^2. \tag{13}$$

Note that in this limit, $\tau \approx 0$ if $\Psi = 1$ due to rapid charge relaxation. We assume that $\Sigma_l \gg 1$ and $\epsilon_l \gg 1$ hereon and discuss the implications of this in Section 3.4.

2.2. Contact line

In this paper, we use the method outlined by Schwartz and Eley [23] to treat the contact line region. This approach involves the 'encoding' of an equilibrium state to which the droplet returns in the absence of any forcing; this then builds in the equilibrium contact angle (in the absence of an electric field) which fixes the height and length scales. The dimensionless version of the disjoining pressure Π in Eq. (5) introduced into the Navier–Stokes equation in Eq. (6) is expressed by (following the suppression of the tildes)

$$\Pi = \frac{B}{h_\infty^n}\left[\left(\frac{h_\infty}{h}\right)^n - \left(\frac{h_\infty}{h}\right)^m\right], \tag{14}$$

in which $B \equiv \mathcal{B}/(\mu\mathcal{U}\mathcal{L}\mathcal{H}^{n-2})$ is a dimensionless parameter which controls the relative significance of disjoining pressure effects. At equilibrium, and in the absence of electric effects, the droplet relaxes to a dimensionless equilibrium shape, taken to be $h = (1-x^2)$, whence $h_x = -2$, at $x = 1$, so that the equilibrium contact angle, $\theta_0 = 2\delta \ll 1$; this is consistent with the lubrication approximation.

Integrating the augmented pressure without electric effects, $p = -h_{xx} - \Pi$, defining the surface energy per unit area as

$$E(h) = -\int_{h_\infty}^{h} \Pi\,\mathrm{d}h, \tag{15}$$

and using a horizontal equilibrium force balance as in [23] one deduces an expression for B in Eq. (14):

$$\Pi = \frac{2(n-1)(m-1)}{(n-m)h_\infty}\left[\left(\frac{h_\infty}{h}\right)^n - \left(\frac{h_\infty}{h}\right)^m\right]. \tag{16}$$

Thus if one releases a droplet away from equilibrium, it then either spreads or undergoes dewetting in order to recover its equilibrium state [23].

A similar approach can be followed in order to determine the effect of electric fields on the equilibrium contact angle. The augmented pressure in the presence of an electric field is given by

$$p = -h_{xx} - \Pi + \frac{\mathcal{C}}{2}\left(\epsilon_l\psi_{lz}^2 - \epsilon_g\psi_{gz}^2\right). \tag{17}$$

An equilibrium force balance in the neighbourhood of the contact line is then carried out by integrating p from h_∞ to a sufficiently large value of h:

$$\int_{h_\infty}^{h} p\,\mathrm{d}h' = -\int_{h_\infty}^{h}\left(h_{xx} + \Pi - \frac{\mathcal{C}}{2}\left[\epsilon_l\psi_{lz}^2 - \epsilon_g\psi_{gz}^2\right]\right)\mathrm{d}h' = 0. \tag{18}$$

Substitution of Eq. (12) into this equation and assuming that Ψ is constant, $h_\infty/h \ll 1$ and $h_\infty/\beta \ll 1$ in the contact line region, we have

$$-\frac{h_x^2}{2} + 2 - \frac{\epsilon_g C\Psi^2 h}{2\beta^2} = 0. \tag{19}$$

We now assume that at equilibrium, with the electric field, there is a new contact angle $\theta_{\rm eq} = -\delta h_x$ $(x = 1)$. However we have specifically non-dimensionalised such that $\theta_0 = 2\delta$. Hence the new contact angle is given by

$$\theta_{\rm eq}^2 = \theta_0^2\left(1 - \frac{\epsilon_g C\Psi^2 h}{4\beta^2}\right), \tag{20}$$

which is Lippmann's result, for small contact angles. In practice, for the simulations undertaken here, $h \sim h_\infty \ll 1$ at the edge and the correction is too small to be detected for the parameter values explored herein.

3. Results

3.1. Numerical procedure

Numerical solutions of Eq. (8) with q, τ and p given by Eqs. (11) and (13) are obtained using a method which utilises finite-element collocation to discretise the spatial derivatives and Gear's method to advance the solution in time [26]. This method has previously been used in related thin film problems [27]. Solutions are determined starting from the following initial conditions

$$h(x,0) = \max\bigl(h_0\bigl(1 - h_0^2x^2\bigr), h_\infty\bigr), \qquad q(x,0) = 0, \tag{21}$$

where $h_0 = 2$ in all the computations. The initial condition for h represents an initially steep drop with a contact angle larger than the equilibrium value. These solutions are obtained subject to the following boundary conditions

$$(h_x, h_{xxx}, q_x)\bigl((0,L),t\bigr) = 0, \tag{22}$$

where L is the length of the computational domain.

The potential at the bottom electrode is given by

$$\Psi(x,t) = 1 + \frac{Sx}{L}\tanh\bigl[B_1(t - B_2)\bigr] + B_3\exp\bigl[-B_4(x - B_5)^2\bigr]. \tag{23}$$

By varying the parameters S and B_1–B_5, we are able to employ a variety of potential forms. For instance, by setting $S = B_3 = 0$, a constant bottom potential is obtained, $\Psi = 1$. A linearly varying spatial dependence can be adopted by setting $B_1 \to \infty$ and $B_3 = 0$ whereas non-zero values for S and B_3 allow for a non-linear spatially-varying potential. The spatial and temporal dependence can thus be altered by changing parameters B_1–B_5 and it will be demonstrated below that this can be used to manipulate the drop in a variety of ways.

Numerical solutions are determined for $0 \leqslant t \leqslant 10^5$ over a wide range of parameters: $2.5 \leqslant \beta \leqslant 10$, $0 \leqslant \mathcal{C} \leqslant 100$, $0 \leqslant B_1 \leqslant 10^2$, $0 \leqslant B_2 \leqslant 10^2$, $0 \leqslant B_3 \leqslant 1$, $0 \leqslant B_4 \leqslant 20$ and $-1 \leqslant B_5 \leqslant 1$; the remaining parameters, i.e., $h_\infty = 0.005$ and $\epsilon_g = 1$ are fixed. Typically, up to 2000 grid points were used to carry out the computations for $L \leqslant 10$.

3.2. Constant potential difference: $\Psi = 1$

We begin our discussion with the simplest form of the applied potential given by Eq. (23) with $S = B_3 = 0$ so that $\Psi = 1$ all along the bottom electrode; as a result, the interfacial shear stress τ due to the electric field is zero. The evolution of the drop height is shown in Fig. 1 with $\mathcal{C} = 1$ and $\beta = 2.5$. The maximal drop height in this case is sufficiently close to the upper electrode initially, which promotes attraction of the interface towards the solid surface. As can be seen in Fig. 1a, the initially convex shape of the drop is drawn upwards forming a sharp 'cone,' until it reaches a distance of 3×10^{-3} from the upper electrode; this is broadly consistent with experimental observations, as shown in Fig. 2. The computations are halted at this point as the spatial derivatives become increasingly singular and difficult to resolve.

The latter stages of the flow, during which the interface approaches the upper electrode, appear to be self-similar and follow a power-law scaling. If t_c denotes the time at which contact between the interface and the electrode occurs then adopting the rescaling $\beta - h(x,t) = \hat{H}(\xi)\hat{t}^{a_1}$ and $x = \xi\hat{t}^{a_2}$ with $\hat{t} = t_c - t$ and noting that local to this contact region, $h \approx \beta$, Eq. (8) becomes

$$\hat{t}^{a_1-1}\bigl[a_1\hat{H} - a_2\xi\hat{H}_\xi\bigr] = \hat{t}^{-2a_2}\frac{\partial^2}{\partial\xi^2}\left(\frac{\beta^3}{3}\left[\hat{t}^{a_1-2a_2}\hat{H}_{\xi\xi} - \frac{\epsilon_g\mathcal{C}}{2\hat{H}^2t^{2a_1}}\right]\right);$$

demanding self-similarity then gives $a_1 = 1/6$ and $a_2 = 1/4$. These scalings are recovered by the numerics, as shown in Fig. 1b. The development of a cone and the apparently self-similar approach of the air–liquid interface towards the upper electrode is reminiscent of other thin film flows involving the formation of singularities; an example of these is finite-time rupture of a thin film driven by van der Waals forces [24]. The coning event occurs very rapidly at the final stages of the experiment and measurements were not accurate enough to verify the theoretical scalings.

If, in contrast, the upper electrode is sufficiently far from the drop initially then the electric force is weak and the drop behaves much as it would in the absence of the electric field: it spreads outwards as $t^{1/7}$, and the maximal height decreases as $t^{-1/7}$, until it approaches an equilibrium; this behaviour is shown in Figs. 1c and 1d. This $t^{-1/7}$ scaling can be obtained by solving the Laplace–Young equation in the longwave limit and imposing volume conservation [23,25]. This is most easily seen by balancing the unsteady and capillary terms in the height evolution equation in the absence of electric and disjoining pressure effects, which yields $x \sim h^{3/4}t^{1/4}$; demanding mass conservation then gives $xh \sim 1$ from which we obtain $x \sim t^{1/7}$ and $h \sim t^{-1/7}$.

3.3. Spatially-varying potential: $\Psi = \Psi(x)$

3.3.1. Linear Ψ variation

We now proceed to investigate the effect of a linear spatially-varying bottom electrode potential, $\Psi = \Psi(x)$, on the dynamics of the spreading drop, noting that the interfacial stress, τ, depends on Ψ and its gradient. In the simulations, we set $B_3 = 0$ so that $\Psi(x) = 1 + Sx$. The rest of the parameters are fixed as $\beta = 5$ and $\mathcal{C} = 1$, and we alter the gradient of the potential

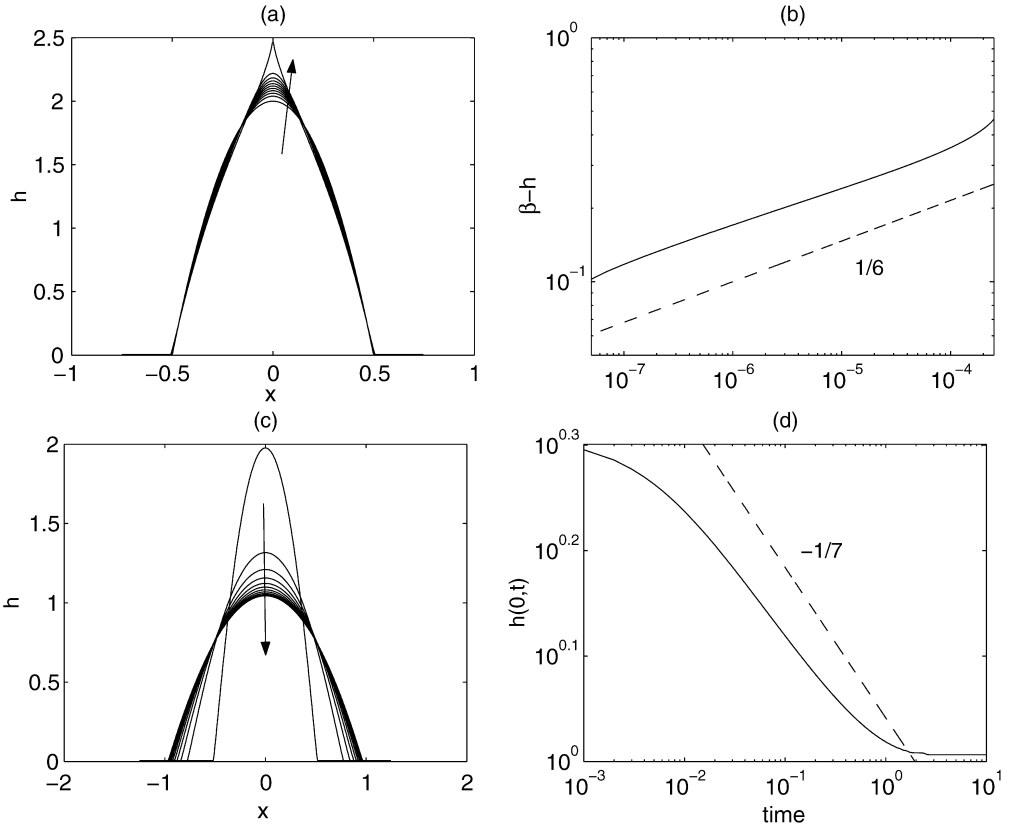

Fig. 1. Typical height evolution for $\Psi = 1$: Panels (a) and (b) have $\beta = 2.5$. Panel (a) shows eleven profiles equally spaced in time from zero to $t_c = 2.49 \times 10^{-4}$ with the arrow showing the direction of increasing time. Panel (b) shows $\beta - h$ versus $\hat{t} = t_c - t$. Panels (c) and (d) have $\beta = 5$; (c) shows the height profiles for $t = 0$ to 1 in time intervals of 0.1 and panel (d) shows the variation of $h(0, t)$ with time. In both computations, $h_\infty = 0.005$ and $h_0 = 2$.

Fig. 2. Image sequences of the coning phenomenon obtained at 1000 fps. A voltage of 2.2 kV was applied across two parallel electrode plates separated by a 5 mm gap, the bottom plate on which a small water drop is placed. The time interval between the images is 1 ms.

by varying the parameter S. Figs. 3a and 3b show the spatio-temporal evolution profiles for the drop height h and the interfacial charge q at dimensionless times $t = 0.1, 1, 50$ for $S = -1$. We observe the drop to undergo an initial transient in which it spreads to its equilibrium state under the action of capillarity up to $t = 1$; the electric stress, arising due to the linear variation in the potential, then acts to translate the drop in the direction of increasing electric field.

The initial spreading transient obeys a capillary scaling law [12,23,25] as shown in Fig. 3c, which demonstrates that $h_{\max} \sim t^{-1/7}$. We note from Fig. 3c that there is a very weak dependence of the duration of this initial capillary spreading transient and $h_{\max}$ on S: the curves associated with $S = -2.5, -5, -10$ are virtually indistinguishable. In contrast, Fig. 3d, in which we plot the temporal evolution of the location of the edge of the drop, x_f, for $S = -2.5, -5, -10$ clearly exhibits three regions. At early times, $x_f \sim t^{1/7}$, since the drop is driven to spread by capillarity. At intermediate times, during which the drop translates under the action of electric stresses, $x_f \sim t^{1/2}$. This can be explained by recalling that, local to the edge of the drop, Ψ is essentially constant and $\beta \gg h$, so that $\tau \sim \epsilon_g \mathcal{C} \Psi^2/(\beta x_f)$, which is balanced by the non-dimensional viscous stress, u_z; a scaling analysis therefore gives

$$\tau \sim \frac{\epsilon_g \mathcal{C}}{\beta x_f} \sim u_z \sim \frac{x_f}{\beta t}, \tag{24}$$

which yields $x_f \sim t^{1/2}$. At late times, as the drop translates over increasingly larger distances, the magnitude of the gradients in the potential diminish and, as a result, electric stresses become weaker; this, then, causes the drop to come to rest. It is also seen in Fig. 3d that the time interval between the early and intermediate-time dynamics decreases with increasing S, which corresponds to larger potential gradients and, therefore, electric stresses.

The interfacial charge q is a measure of the normal electric stress in the gas phase acting on the interface. Although Ψ is a linear function of x, we note that the interfacial charge and the pressure are inversely proportional to $\beta - h$, as given by Eqs. (11) and (13), respectively. The drop translation towards the region of low electric stress is therefore a consequence of

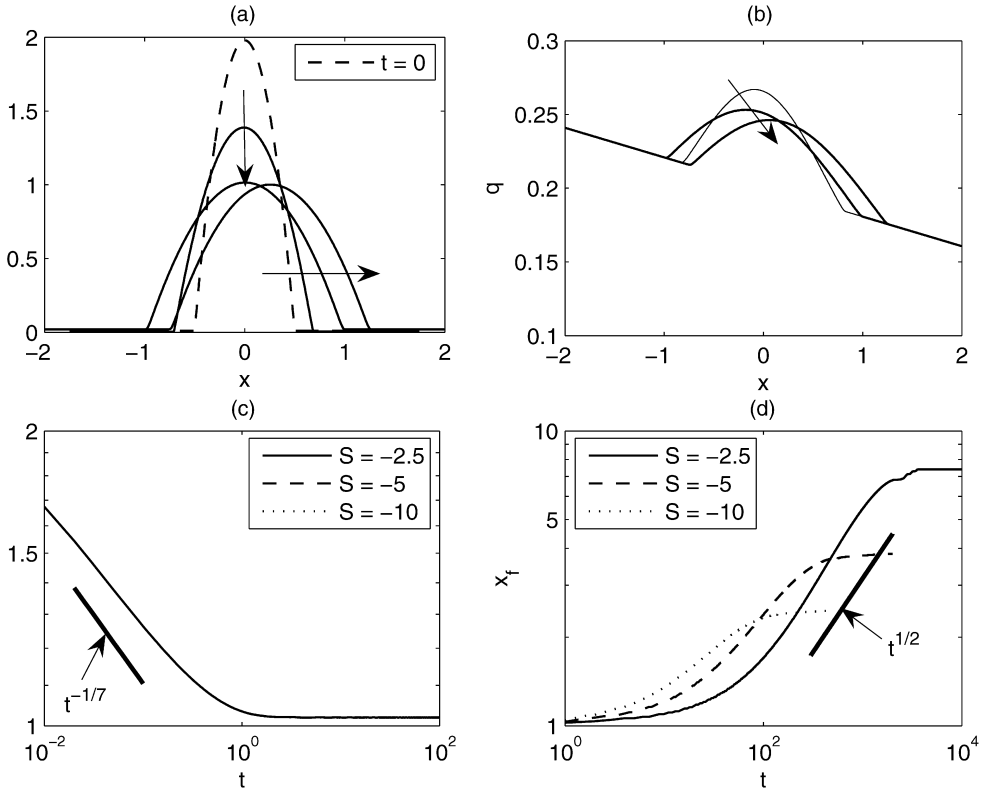

Fig. 3. Typical spatio-temporal evolution of (a) the drop height, and (b) the interfacial charge, for a linear spatially-varying potential, $\Psi = 1 + Sx$, with $S = -1$ at times $t = 0, 0.1, 1$ and 50. Panels (c) and (d) indicate the corresponding decrease in the maximum drop height $h_{\max}$ (the curves are so close as to almost appear indistinguishable for $h_{\max}$) and the position of the advancing drop front x_f as a function of time for various values of the gradient S. In all computations, the system parameters are fixed at $\beta = 5$ and $\mathcal{C} = 1$; only the gradient S was varied.

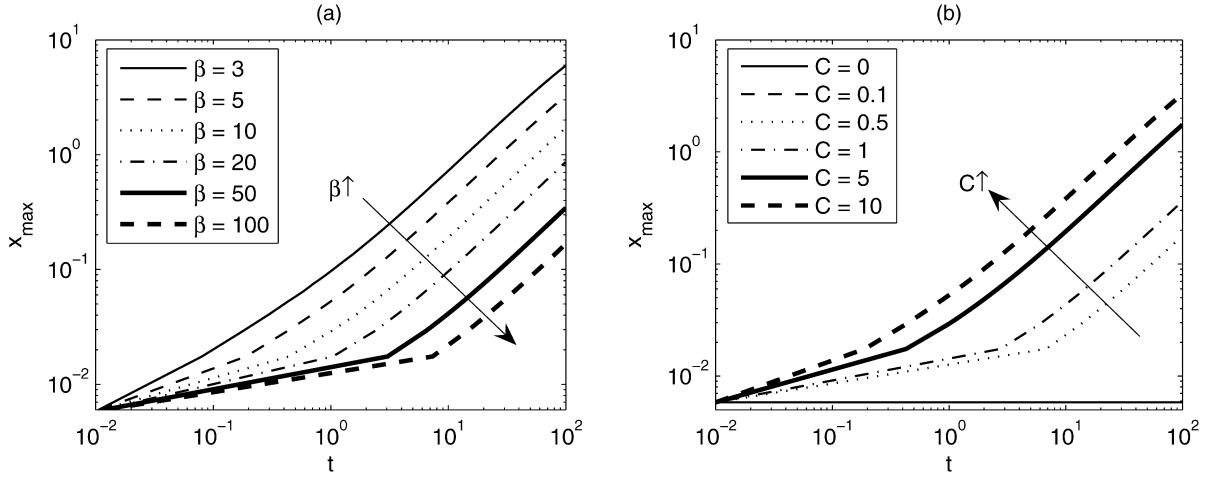

Fig. 4. Effect of (a), the electrode separation β, and (b), the electric capillary number $\mathcal{C}$ on the drop position, defined by the maximum drop height, $x_{\max}$. When β and $\mathcal{C}$ are varied, we set $\mathcal{C} = 10$ and $\beta = 5$, respectively.

a positive pressure gradient squeezing bulk liquid in the drop towards regions in the drop which suffer a lower interfacial electric stress.

The drop translation speed is also a function of the electrode separation β. This can be seen more clearly if the position of the drop vertex, $x_{\max}$, is plotted, since $x_{\max} > 0$ only if the electric field acts to translate the drop. As shown in Fig. 4a, the onset of drop translation is delayed significantly with increasing β because there is insufficient electric stress to overcome the capillary stress required to induce translational motion. At large β values, the drop simply spreads to an equilibrium contact angle and decreasing β serves to increase the drop propagation speed. We also observe in Fig. 4b the existence of a critical value of approximately $\mathcal{C} = 0.1$ for the electric capillary number for drop translation to take place for this set of parameter values. Below this value, the magnitude of electric stresses is insufficient to drive drop translation.

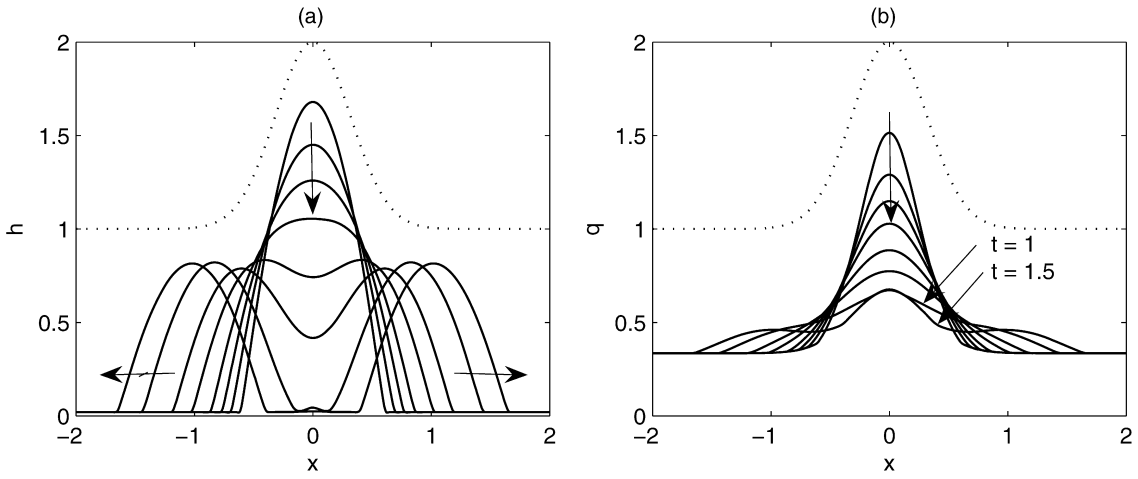

Fig. 5. Typical spatio-temporal evolution of (a) the drop height, and (b) the interfacial charge, for a non-linear spatially-varying potential at $t = 0.01, 0.025, 0.05, 0.1, 0.25, 0.5, 1$ and 1.5. In all computations, the system parameters are fixed at $S = 1$, $\beta = 3$, $\mathcal{C} = 10$, $B_1 = 0$, $B_2 = 10$, $B_3 = 1$, $B_4 = 5$ and $B_5 = 0$. The spatially-varying potential, Ψ, given by Eq. (23) with the parameters above is shown by the dotted lines.

3.3.2. *Non-linear Ψ variation and drop surgery*

Non-linear spatial and temporal variations in the potential can be examined by isolating the effects of each of the parameters B_1–B_5 in Eq. (23). The 'base' parameter set is $B_1 = 0$, $B_2 = 10$, $B_3 = 1$, $B_4 = 5$ and $B_5 = 0$. All but one of these parameters are held constant on each run to determine the role of the said parameter on the drop dynamics. The other system parameters are held constant, i.e., $\beta = 3$, $\mathcal{C} = 10$, and $S = 1$. Typical spatio-temporal evolution profiles of the film height and the interfacial charge are shown in Figs. 5a and 5b, respectively. It can be seen from Fig. 5a that the drop spreads symmetrically under the action of capillarity as was also seen with the linearly varying potentials. However, after a short transient, the center of the drop at $x = 0$ begins to thin more rapidly than its sides (the profile shown when the drop begins to split is at $t = 0.5$). When $h(0, t)$ becomes approximately equal to h_∞ at $t = 1$, two secondary drops are formed that proceed to translate in opposite directions leaving behind a very small liquid droplet at the center which does not persist.

The wetting and thinning behaviour is closely related to the interfacial charge evolution. Clearly, due to the symmetry in the interfacial charge, as shown in Fig. 5b, the region of highest normal gas phase interfacial electric stress is at the drop center whereas the region of lowest stress is at the periphery of the drop. This gives rise to a pressure gradient that is directed away from the center which acts to thin the drop at the flow origin and promotes 'dewetting.' The eventual splitting of the primary drop into two secondary drops occurs because the normal electric stress gradient at the center is too strong and squeezes the drop in the center more than the drop can overcome viscous effects at the outer contact line where the normal electric stress gradient is weak. This causes the drop to thin in the center much faster than the drop can translate outwards. Although the overall shape of the q profiles is similar to that of h, as expected from Eq. (11), there develops a ridge in q local to the origin and 'shoulders' that are spatially co-incident with the translating secondary drops before a value of $q = \epsilon_g/(\beta - h) \approx 1/3$ for large x is reached. We also note that the magnitude of the charge at the center remains essentially constant once the film has completely 'dewetted.'

Similar to the case of a linear Ψ in Section 3.3.1, there also exists a critical condition for the drop splitting to occur. Fig. 6a shows the drop height at the center, $h(0, t)$, for different values of β. It can be seen that splitting occurs for β values below $\beta \approx 6.5$ for this set of parameters. Above this value, at $\beta = 7$, for instance, $h(0, t) \sim t^{-1/7}$ due solely to capillarity. Below $\beta \approx 6.5$, the drop height decreases rapidly after the initial capillary spreading transient towards h_∞, at which dewetting at the drop center occurs, as shown in Fig. 6a. We also note in Fig. 6a slight increase in $h(0, t)$ which is due to the small liquid drop remnant at the center. This is not evident for $\beta \geqslant 5$ for this set of parameters.

The effect of varying $\mathcal{C}$ on the temporal evolution of $h(0, t)$ is shown in Fig. 6b. Again, a critical value of $\mathcal{C} \approx 5$ exists, below which the electric stresses are insufficient to overcome the capillary stresses and cause splitting; the drop, in this case, relaxes towards an equilibrium position with a static contact angle determined by the Lippmann equation. As shown in the inset of Fig. 6b, which plots the drop profile at long times, up to $t = 500$ for $\mathcal{C} = 1$, no further spreading occurs once this static contact angle is reached. This is akin to static electrowetting in which the static contact angle is determined solely by a force balance at the contact line, which accounts for electric stress [12,25] (see Section 2.2). However, above the critical electric capillary number, the rich dynamics of translation and splitting discussed above are observed.

The asymmetry of the drop can be controlled by the parameter B_5. We show in Figs. 7a and 7b that a smaller drop is formed in the $x < 0$ ($x > 0$) plane for $B_5 < 0$ ($B_5 > 0$). Figs. 7c and 7d also demonstrate the existence of a critical B_5 value, $B_5 \approx 1$, for splitting of the primary drop into two secondary drops. Above this critical value, no secondary drops are formed. In a manner similar to that observed in the case of linear spatial potentials, the drop simply spreads by capillarity and subsequently translates. The position of the drop and the direction of its translation, however, again depend on the sign of B_5.

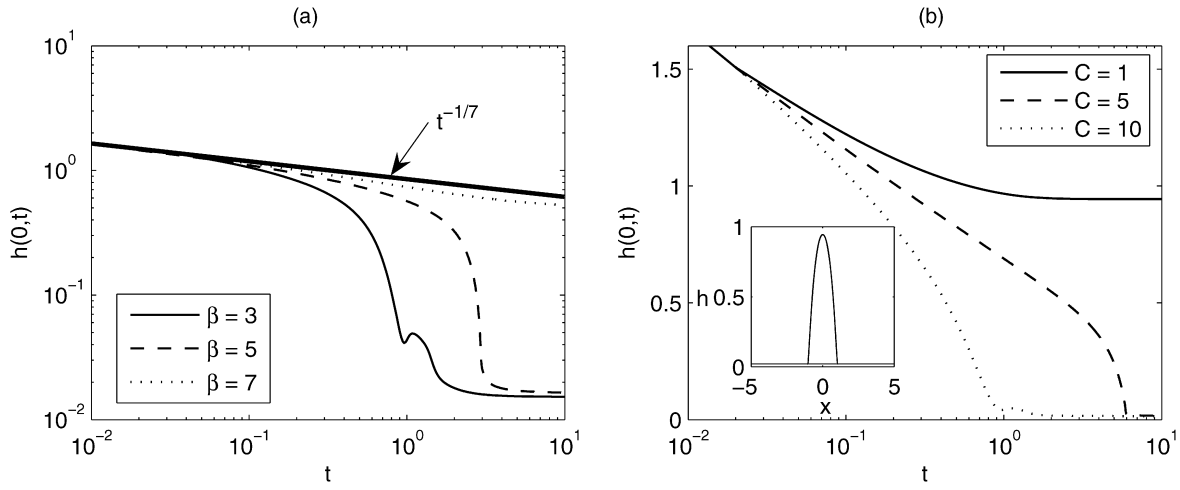

Fig. 6. Transient behaviour of $h(0,t)$ for various values of (a) the electrode separation β, and (b) the electric capillary number $\mathcal{C}$. The inset in (b) shows the drop profile for $\mathcal{C}=1$ at long times up to $t=500$, demonstrating that once equilibrium conditions are reached, there is no further spreading. The remaining system parameters are $S=1$, $B_1=0$, $B_2=10$, $B_3=1$, $B_4=5$ and $B_5=0$. When variations in β and $\mathcal{C}$ are considered, we set $\mathcal{C}=10$ and $\beta=3$, respectively.

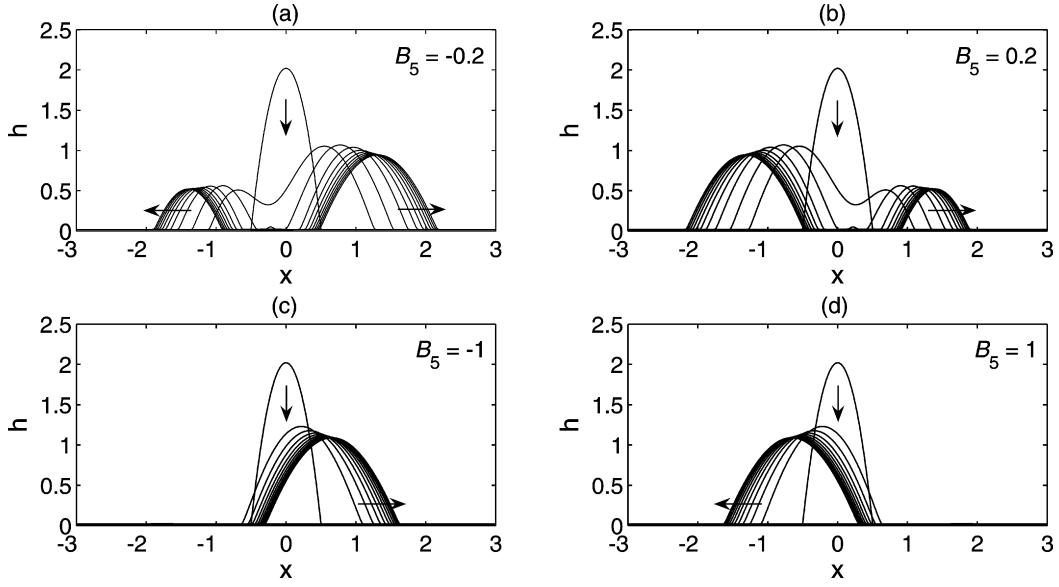

Fig. 7. Effect of varying the parameter B_5 on the evolution of the drop height. Profiles are shown for 10 equal time steps up to $t=5$. Below $|B_5|\sim 1$, secondary drops are produced when the primary drop splits due to dewetting. Above this magnitude, no splitting occurs and only translation of the primary drop results. The other system parameters are $S=1$, $\beta=3$, $\mathcal{C}=10$, $B_1=0$, $B_2=10$, $B_3=1$, and $B_4=5$.

3.3.3. Complex drop manipulation

We explore briefly possible ways of manipulating the drops further by varying the parameters in the base potential in Eq. (23). For example, by decreasing B_4 by an order of magnitude to 0.5, it is possible to widen the base of the small remnant of liquid that is left behind at the center at $x=0$ when the film finally dewets on both its sides, as illustrated in Fig. 8a. As a consequence, another pair of secondary drops are formed from the liquid remnant (see Fig. 8b) near the flow origin. Thus, four drops can be produced. It can also be seen from Fig. 8c that the smaller drops travel outwards much faster than the larger drops at the periphery. They eventually catch up with the larger drops and remerge, as seen in Fig. 8d.

It is also possible to arrest the translation of one secondary drop whilst allowing the other secondary drop to continue translating. This is shown in Fig. 9a where we set B_1 to be non-zero only when $t>t_b$, where $t_b=1$. Fig. 9b shows that the opposite occurs when the sign on B_1 is reversed. The time at which one of the drops begins to be retarded, can be delayed by increasing t_b.

Finally, we show the possibility of drop splitting and recombination in Fig. 10. This is performed by first splitting the drop using the non-linear spatial potential distribution used to generate Fig. 5, i.e., Eq. (23) with the 'base' parameters $B_1=0$, $B_2=10$, $B_3=1$, $B_4=5$ and $B_5=0$ with $S=-1$ for $t<10$, and then via translation of the daughter drops towards each other using the linear spatial potential distribution, i.e., Eq. (23) with $B_1\to\infty$, $B_2=10$, $B_3=0$, $B_4=5$ and $B_5=0$ with $S=2$ for $t\geqslant 10$; the gradient S was doubled in order to speed up the recombination process. It should be noted, however, that the

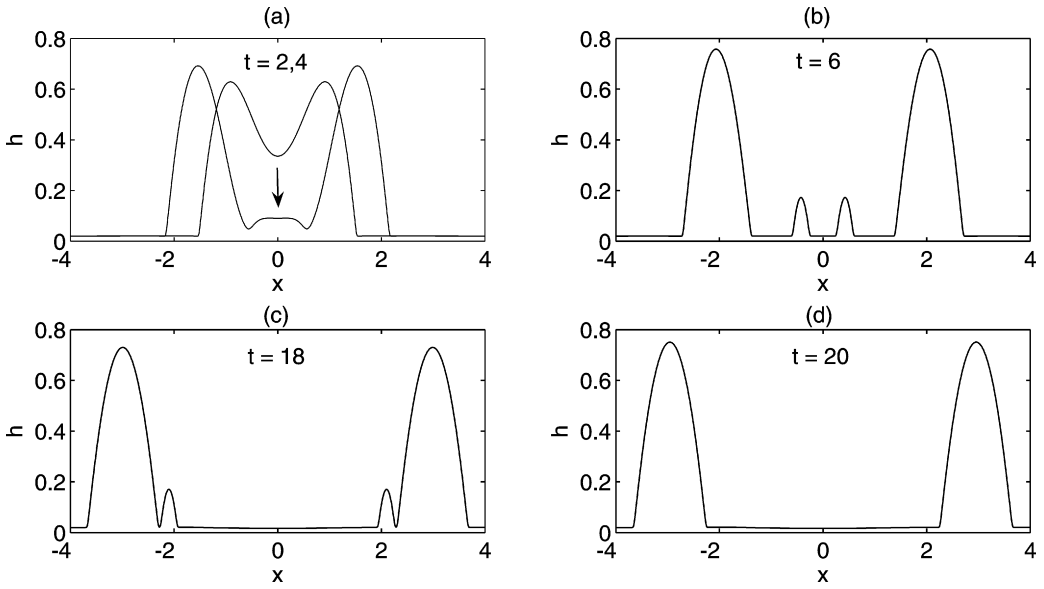

Fig. 8. Drop height profiles at various times when $B_4 = 0.5$, showing the formation of two additional secondary drops which translate outwards faster than the larger peripheral drops. Eventually the small drops catch up with the larger drops and merge with them. The rest of the system parameters are $S = 1$, $\beta = 3$, $\mathcal{C} = 10$, $B_1 = 0$, $B_2 = 10$, $B_3 = 1$ and $B_5 = 0$.

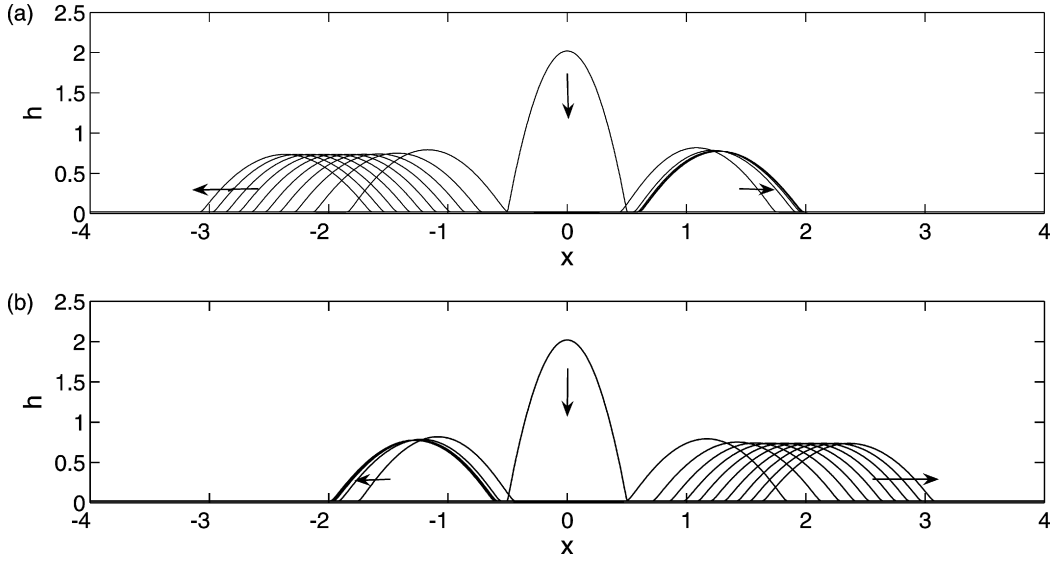

Fig. 9. Effect of the delayed introduction of a non-zero value of B_1 after $t = t_b$. Panels (a) and (b) show the drop height evolution profiles for 10 equal time steps up to $t = 20$ for $B_1 = 10$ and $B_1 = -10$, respectively, when $t_b = 1$. The remaining system parameters are $S = 1$, $\beta = 3$, $\mathcal{C} = 10$, $B_2 = 10$, $B_3 = 1$, $B_4 = 5$ and $B_5 = 0$.

absolute value of x is required, i.e., the linear term in Eq. (23) reads $S|x|/L$, such that both daughter drops translate towards each other; they then merge to form a single drop which comes to rest with an equilibrium shape.

3.4. Model limitations and connection to experiments

The theory developed in this paper to model the spreading, splitting, translation and recombination of a drop in the presence of electric fields suffers from a number of limitations. First, the lubrication approximation was used to simplify the governing equations which facilitated the derivation of a pair of coupled evolution equations for the film thickness, h, and interfacial charge density, q. Implicit in this approach is the assumption of a slender droplet and therefore a separation of scales between the horizontal and vertical length scales. The validity of this assumption, however, is called into question in such situations as those wherein the drop is attracted by the top electrode in order to form a Taylor-like cone. It is far from clear that a separation of scales exists for such situations particularly as contact between the air–liquid interface and the top electrode is approached: $h \sim \hat{t}^{1/6}$ and $x \sim \hat{t}^{1/4}$ so that $h_x \sim \hat{t}^{-1/12}$ ($\hat{t} = t_c - t$), suggesting that h_x diverges as $t \to t_c$.

It is also important to note the approximations made regarding electric field effects. We have assumed electroneutrality within the bulk of the fluid drop, constant permittivities, the electric fields to be solenoidal and irrotational and neglected conduction along the interface. We have also assumed the mag-

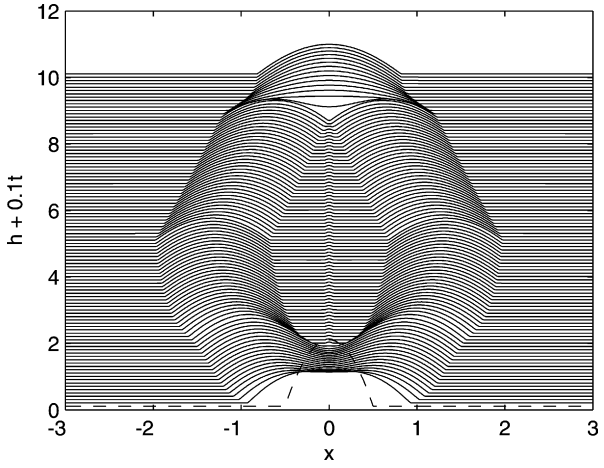

Fig. 10. Space–time plots of the film thickness showing the possibility of drop splitting and recombination. The potential used is given by Eq. (23) with $B_1 = 0$, $B_2 = 10$, $B_3 = 1$, $B_4 = 5$ and $B_5 = 0$ with $S = -1$ for $t < 10$ and $B_1 \to \infty$, $B_2 = 10$, $B_3 = 0$, $B_4 = 5$ and $B_5 = 0$ with $S = 2$ for $t \geqslant 10$. The other system parameters are $\beta = 5$ and $\mathcal{C} = 10$. The dotted line shows the initial drop profile.

netic time scales to be much shorter than those associated with electric effects. These assumptions are consistent with the leaky dielectric model [28]. At high voltages, however, it is possible that a number of the above-mentioned assumptions may become invalid (such as, for instance, the electroneutrality assumption) and the model would have to be modified appropriately in these cases.

In addition, we have assumed that the electric conductivity and the fluid dielectric constant are large, namely $\sigma_l \mathcal{L}/\epsilon_0 \mathcal{U} = \Sigma_l \gg 1$ and $\epsilon_l \gg 1$, respectively, which permitted the decoupling of Eqs. (8) and (9); this also allowed us to determine q via knowledge of h through Eq. (11). Typically, liquid conductivities of electrolytes range between 10^{-6}–10 S/m^2 such that $\Sigma_l \sim 10^5$–10^{12}. The assumptions may thus be permissible for electrolytes like water, alcohols and other aqueous solutions but would be questionable for others such as deionised water and organic liquids for which charge relaxation time scales may be comparable to those of the flow and the dielectric constant may be of order unity. We also note that the Reynolds number $Re \equiv \rho \mathcal{U} \mathcal{H}/\mu \sim 10^{-1}$ and hence $\delta Re \sim 10^{-3}$ so that the lubrication approximation is not rendered invalid.

It is also important to establish a tentative connection between our modelling predictions of drop surgery and manipulation (see, for instance, Fig. 10), which are based on various forms of the spatio-temporally varying bottom potential, $\Psi(x, t)$, and practical implementations of these strategies in laboratory experiments. Such could possibly involve elegant patterning of the electrode surfaces through the various schemes suggested earlier in Section 1. One method that shows promise for producing non-linear spatial potentials is the tuning of the localised zeta potential at the substrate surface through field effects, as proposed by Schasfoort et al. [16]. Thin Au/Cr films are deposited or injected within an insulating substrate to form buried shielding electrodes in order to generate capacitance effects which in turn results in a redistribution of the surface potential when subjected to an applied voltage. By reducing the width and spacing of successive electrodes, an almost continuous potential distribution can be obtained. Temporal variations can then be superimposed through clever control schemes.

4. Conclusions

In this paper, we have studied the dynamics of a liquid drop on a solid substrate in the presence of an electric field. We have used lubrication theory to derive coupled evolution equations for the film thickness and interfacial charge density. In the limit of large liquid conductivity, the electric field effects are confined to the gas phase and hence the governing equations can be simplified further to give a single evolution equation for the film thickness; the interfacial charge density is enslaved adiabatically to the height in this limit. We show through numerical simulations that a conducting liquid drop sandwiched between bottom and top electrodes with a small air gap above the drop can be manipulated by electrowetting schemes that employ spatial and temporal potential distributions.

Several different potential distributions for the bottom electrode have been explored. When the potential is constant and the electrode separation and hence the air gap above the drop is sufficiently small, a Taylor-like conical drop is observed. We have shown that, in this case, the maximal drop height evolves in a self-similar manner as the drop approaches the top electrode. If a spatially linear potential distribution is employed, the drop is observed to initially spread due to pure capillary action. For weak electric fields, no further spreading occurs after an equilibrium contact angle condition is reached. This is also true for the constant potential case when the electric field is weak. However, above a critical electric capillary number and/or below a critical separation, the drop translates in the direction of increasing field intensity whilst maintaining its overall shape and contact angle. The translation speed can be increased by increasing the gradient of the linearly varying potential.

More interesting, however, is the case of a non-linear potential distribution in which the splitting of the drop is observed, again beyond a critical condition. Both symmetric and asymmetric splitting were shown to be possible by controlling various parameters in the potential distribution. Furthermore, additional secondary drops can be generated, which can also be recombined with the primary daughter drops which have split off from the mother drop. We have also demonstrated various other complex drop manipulation schemes by introducing temporal variations to the non-linear spatial potential distribution: splitting of the drops followed by translation of one daughter drop but halting the other daughter drop as well as the splitting of the drops followed by their recombination.

These electrowetting schemes for drop surgery and manipulation are very useful for various microfluidic devices in which precise drop control is required. The possibility of such schemes as shown through these speculative numerical experiments are intended to inspire experimental work based on the models employed here.

Acknowledgments

O.K.M. would like to thank the EPSRC for their support through Grant No. EP/D50371X. L.Y.Y. was supported by an ARC Discovery Grant DP0666549. The experimental images in Fig. 2 were obtained with the help of Mr. Wilson Tan. L.Y.Y. also wishes to thank Dr. James Friend at Monash University for helpful discussions on electrode fabrication.

References

[1] T.M. Squires, S.R. Quake, Rev. Mod. Phys. 77 (2005) 977.
[2] M.W.J. Prins, W.J.J. Welters, J.W. Weekamp, Science 291 (2001) 277.
[3] F. Mugele, J.-C. Baret, J. Phys. Condens. Matter 17 (2005) R705.
[4] M.G. Pollack, A.D. Shenderov, R.B. Fair, Lab Chip 2 (2002) 96.
[5] S.K. Cho, H. Moon, C.-J. Kim, J. Microelectromech. Syst. 12 (2003) 70.
[6] R. Digilov, Langmuir 16 (2000) 6719.
[7] T.B. Jones, J.D. Fowler, Y.S. Chang, C.-J. Kim, Langmuir 19 (2003) 7646.
[8] T.B. Jones, K.L. Wang, D.J. Yao, Langmuir 20 (2004) 2813.
[9] M. Vallet, M. Vallade, B. Berge, Eur. Phys. J. B 11 (1999) 583.
[10] K.H. Kang, Langmuir 18 (2002) 10318.
[11] J. Buehrle, S. Herminghaus, F. Mugele, Phys. Rev. Lett. 91 (2003) 086101.
[12] L.Y. Yeo, H.-C. Chang, Mod. Phys. Lett. B 19 (2005) 549.
[13] Z. Gagnon, H.-C. Chang, Electrophoresis 26 (2005) 3725.
[14] J.S. Bader, J.M. Rothberg, G.T. Mulhern, M.W. Deem, G.T. Went, S. Henck, J. Simpson, Can. Pat. CA 2354589A1, 2000.
[15] M.A. Hayes, I. Kheterpal, A.G. Ewing, Anal. Chem. 65 (1993) 2010.
[16] R.B.M. Schasfoort, S. Schlautmann, J. Hendrikse, A. van den Berg, Science 286 (1999) 942.
[17] N.A. Polson, M.A. Hayes, Anal. Chem. 72 (2000) 1088.
[18] C.-Y. Lee, G.-B. Lee, L.-M. Fu, K.-H. Lee, R.-J. Yang, J. Micromech. Microeng. 14 (2004) 1390.
[19] G.-B. Lee, L.-M. Fu, C.-H. Lin, C.-Y. Lee, R.-J. Yang, Electrophoresis 25 (2004) 1879.
[20] R.M. White, F.M. Volmer, Appl. Phys. Lett. 7 (1965) 314.
[21] A.V. Mamishev, K. Sundara-Rajan, F. Yang, Y. Du, M. Zahn, Proc. IEEE 92 (2004) 808.
[22] R.V. Craster, O.K. Matar, Phys. Fluids 17 (2005) 032104.
[23] L.W. Schwartz, R.R. Eley, J. Colloid Interface Sci. 202 (1998) 173.
[24] W.W. Zhang, J.R. Lister, Phys. Fluids 11 (1999) 2454.
[25] L.Y. Yeo, H.-C. Chang, Phys. Rev. E 73 (2006) 011605.
[26] P. Keast, P.H. Muir, ACM. Trans. Math. Software 17 (1991) 153.
[27] M.R.E. Warner, R.V. Craster, O.K. Matar, J. Fluid Mech. 510 (2004) 169.
[28] D.A. Saville, Ann. Rev. Fluid Mech. 29 (1997) 27.